CERAMICS
INTERNATIONAL

Optical and electrochemical properties of perovskite type MAlO$_3$ (M=Y, La, Ce) pigments synthesized by a gamma-ray irradiation assisted polyacrylamide gel route

Huajing Gao[a,b], Hua Yang[a,b], Shifa Wang[c,d,*], XinXin Zhao[a,b]

[a] State Key Laboratory of Advanced Processing and Recycling of Non-ferrous Metals, Lanzhou University of Technology, Lanzhou 730050, China
[b] School of Science, Lanzhou University of Technology, Lanzhou 730050, China
[c] Science and Technology on Vacuum Technology and Physics Laboratory, Lanzhou Institute of Physics, Gansu, Lanzhou 730000, China
[d] Institute of Nuclear Physics and Chemistry, China Academy of Engineering Physics, Sichuan, Mianyang 621900, China

ABSTRACT

Perovskite type MAlO$_3$ (M=Y, La, Ce) pigments with different phases were successfully prepared by a gamma-ray irradiation assisted polyacrylamide gel route under the same synthesis conditions and their phase purity, surface morphology, and color, optical, photoluminescence and electrochemical properties were characterized by X-ray diffraction (XRD), UV–visible spectroscopy (UV–Vis), field-emission scanning electron microscopy (FE-SEM), transmission electron microscopy (TEM), fluorescence spectroscopy (FS), and electrochemical impedance spectroscopy (EIS). The effects of crystallization temperature and trivalent metal ion M^{3+} on the physico-chemical properties of MAlO$_3$ (M=Y, La, Ce) pigments were systematically investigated. The crystallization temperature of MAlO$_3$ pigments decreases with the increasing ion radius of trivalent metal ions M^{3+}. The synthetic route produced nanosized or porous powders, in addition, no direct relationship was resulted between particle size or energy band gap (Eg) value of MAlO$_3$ pigments with trivalent metal ions M^{3+}. Among all, CeAlO$_3$ and YAlO$_3$: Ce pigments exhibited excellent photoluminescence properties, in which the emission peaks at 378, 429, 468 and 480 nm with the excitation wavelength at 280 nm and the emission peaks at 369, 413 and 458 nm with the excitation wavelength at 270 nm, respectively. The fluorescence mechanism of the CeAlO$_3$ and YAlO$_3$: Ce pigments were studied based on previous reports and the experimental results. The color and electrochemical properties of MAlO$_3$ pigments change appears to be highly dependent on the trivalent metal ions M^{3+}. Moreover, the results demonstrated that doping Ce^{3+} ions into YAlO$_3$ precursor solution dropped crystallization temperature and improved phase purity, photoluminescence, and electrochemical properties of YAlO$_3$ pigment.

1. Introduction

Perovskite type oxides with ABO$_3$ structure are of intense interests in science and technology research due to their outstanding physico-chemical properties and widespread applications in industry and academia [1–4]. Among these, rare earth aluminates (MAlO$_3$; M=Sc, Y and lanthanide) have recently attracted considerable attention by virtue of their superior mechanical, thermal, magnetic, optical, electrical, catalytic properties and tremendous potential applications in white LEDs and scintillators [5], laser [6], quantum oscillator [7], catalysts [8], pigments [9], and so on. Recently, rare earth aluminate pigments has attracted considerable attention because of their low toxicity and environment-friendly pigment when compared to the conventional pigment [9]. Color properties of the (La, Pr, Nd)AlO$_3$

pigments were already reported in literature [9], but to the best of our knowledge, no publications are presenting the color properties of the (Y, Ce)AlO$_3$ pigments. It is well known that the LaAlO$_3$ pigment is very stable due to the Laporte forbidden 4f-4f electronic transitions in the LaAlO$_3$ crystal [10]. To understand the electronic band structure and the photoelectric properties of MAlO$_3$ (M=Y, La, Ce) pigments, the flat band potential (Vfb), electrochemical impedance spectroscopy and photocurrent response are very useful parameters for the study the electrochemical properties of MAlO$_3$ (M=Y, La, Ce) pigments. However, the electrochemical properties of MAlO$_3$ (M=Y, La, Ce) pigments have not yet been reported. By comparing the LaAlO$_3$ pigment, it is interesting to study the color and electrochemical properties of the (Y, Ce)AlO$_3$ pigments.

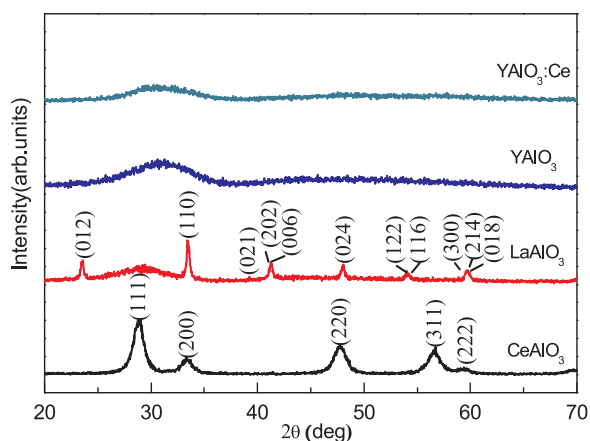It is also well known that the cerium ion (Ce^{3+}) have a 4f

Fig. 1. XRD patterns of the MAlO$_3$ (M = Y, La, Ce) and YAlO$_3$: Ce xerogels calcined at 700 °C.
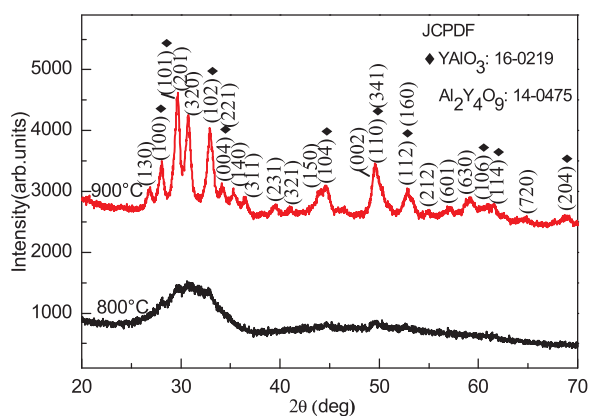

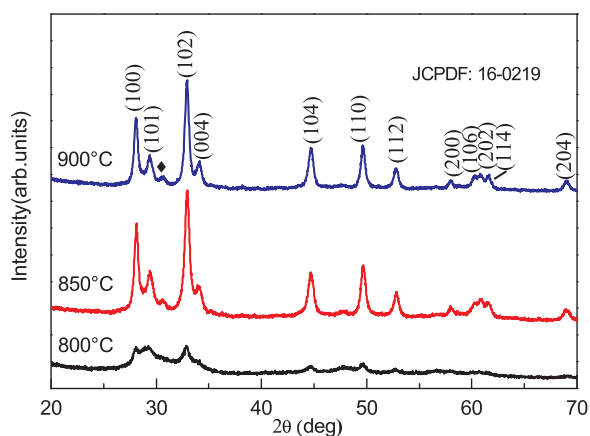**Fig. 2.** XRD patterns of the YAlO$_3$ xerogels calcined at 800 and 900 °C.

Fig. 3. XRD patterns of the YAlO$_3$: Ce xerogels calcined at 800, 850 and 900 °C.

configuration is spin-allowed 4*f*–5*d* transition [11]. Therefore, it is expected to developing a strategy to obtain multi-color emitting phosphors by doping Ce^{3+} ions in the rare earth aluminate pigments. To generate multi-color emission from rare earth aluminate pigments, synthetic route have been playing an important role due to the physico-chemical properties were significantly associated with the preparation method [12–16]. As of now, a variety of different methods, such as the sol-gel method [8,17], the hydrothermal method [18,19], the Pechini

method [20], the combustion synthesis method [21–24], the solid-state reaction method [25], the co-precipitation method [26,27], a modified polymeric precursors method [28], the impregnation method [29], and the polyacrylamide gel method [30,31], have been used to manipulate the shapes and sizes of the MAlO$_3$ (M = Y, La, Ce) pigments. Among these methods, the polyacrylamide gel method is a promising preparation method that the phase purity, crystalline morphology, and physico-chemical properties of target products can be well-controlled by adjusting the experiment parameters [32–34]. Recently, the polyacrylamide gel route have been improved on the basis of γ- ray irradiation to initiate the polymerization of acrylamide and *N*,*N*′-methylene-bisacrylamide in the precursor solution [35,36]. Low cost, eco-friendly reagent, mild reaction condition, smaller particle size, and special defect structure are the advantages of gamma-ray irradiation assisted polyacrylamide gel route.

In this article, the perovskite type MAlO$_3$ (M = Y, La, Ce) pigments were synthesized by a gamma-ray irradiation assisted polyacrylamide gel route. The effects of crystallization temperature and trivalent metal ion M^{3+} on the phase purity, surface morphology, color, optical, photoluminescence, and electrochemical properties of the MAlO$_3$ (M = Y, La, Ce) pigments were evaluated. The objective of the present work is to study the relationship between the color, optical, photoluminescence, or electrochemical properties of the MAlO$_3$ (M = Y, La, Ce) pigments and trivalent metal ion M^{3+}. The fluorescence mechanism of the CeAlO$_3$ and YAlO$_3$: Ce pigments have been discussed on the basis of the crystal field theory and the experimental result.

2. Experimental

2.1. Synthesis of MAlO$_3$ (M = Y, La, Ce) nanoparticles

According to the formula MAlO$_3$, stoichiometric amounts of Y (NO$_3$)$_3$·6H$_2$O (99%), La(NO$_3$)$_3$·6H$_2$O (99%) or Ce(NO$_3$)$_3$·6H$_2$O (99%), and Al(NO$_3$)$_3$·9H$_2$O (99.5%) were dissolved in the deionized water to obtain a solution of 0.015 mol/L. After the solution was transparent, a stoichiometric amount of chelating agent (citric acid (C$_6$H$_8$O$_7$, 99.5%)) was added to the solution to complex the cations in the molar ratio 1.5:1 with respect to the cations (Y, La, Ce or Al). After that, 20 g glucose (C$_6$H$_{12}$O$_6$.H$_2$O, 99%) was dissolved in the solution. Finally, the acrylamide (C$_3$H$_5$NO, AR) and N, N′-methylene-bisacrylamide monomers (C$_7$H$_{10}$N$_2$O$_2$, 99%) were added to the solution and the pH value was adjusted to 3 with aqueous ammonia solution. The total amount of monomers for each case was 9 times (mole amount) of that of cations. The resultant solution was placed in glass ampoule and was exposed to ^{60}Co γ-source (China- China Academy of Engineering Physics, ^{60}Co γ-ray irradiation apparatus) at a dose of 20 kGy to initiate the polymerization reaction. The gel was dried at 120 °C for 24 h in a thermostat drier. The obtained xerogel precursor was ground into powder and some powder was calcined for 5 h in air at different temperatures to obtain the products.

2.2. Synthesis of YAlO$_3$: Ce nanoparticles

According to the formula YAlO$_3$: Ce (n_{Ce}:n_{Y+Al} = 1:9), stoichiometric amounts of Y(NO$_3$)$_3$·6H$_2$O, Ce(NO$_3$)$_3$·6H$_2$O, and Al(NO$_3$)$_3$·9H$_2$O were dissolved in the deionized water to obtain a solution of 0.015 mol/L. After the solution was transparent, a stoichiometric amount of chelating agent (citric acid) was added to the solution in the molar ratio 1.5: 1 with respect to the cations (Al) to complex the cations. Finally, the YAlO$_3$: Ce nanoparticles can be synthesized according to Section 2.1.
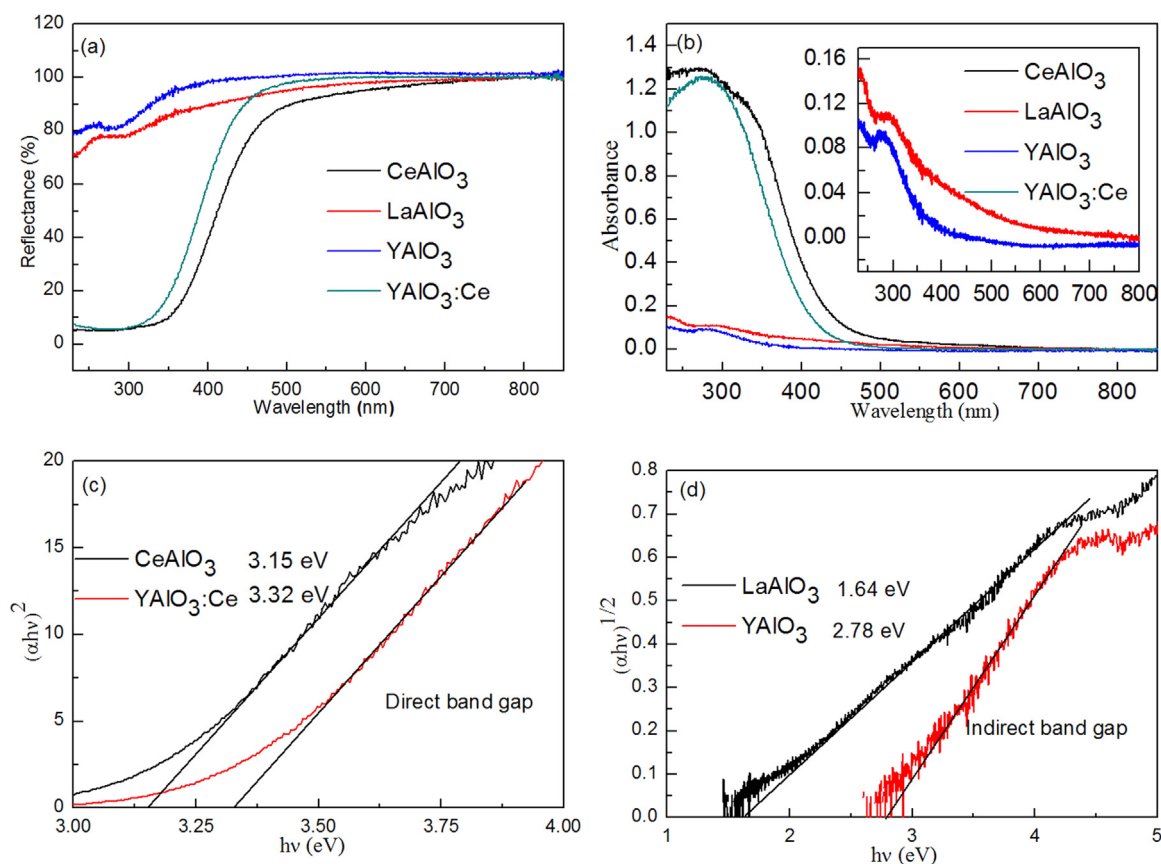
Fig. 4. (a) UV–vis diffuse reflectance spectra, (b) UV–Vis absorption spectra of the $MAlO_3$ (M = Y, La, Ce) and $YAlO_3$: Ce xerogels calcined at 700 °C. The inset presents the enlarged drawing of UV–Vis absorption spectra of the $LaAlO_3$ and $YAlO_3$ xerogels calcined at 700 °C. The optical band gap (Eg) values of (c) $CeAlO_3$ and $YAlO_3$: Ce, (d) $LaAlO_3$ and $YAlO_3$ xerogels calcined at 700 °C.

Table 1
Color coordinates and Eg values of the $CeAlO_3$, $LaAlO_3$, $YAlO_3$ and $YAlO_3$: Ce xerogels calcined at different temperatures.

Sample	Temperature (°C)	Color coordinates						Eg value (eV)
		L*	a*	b*	c*	H°	ΔE_{CIE}^{*}	
$CeAlO_3$	700	96.05	−2.95	13.39	13.71	−77.58	97.02	3.15
$LaAlO_3$	700	97.92	0.06	2.92	2.92	88.82	97.96	1.64
$YAlO_3$	700	99.71	−0.04	1.01	1.01	−87.73	99.72	2.78
	800	98.36	0.05	0.93	0.93	86.92	98.36	2.73
	900	99.24	−0.39	1.81	1.85	−77.84	99.26	2.50
$YAlO_3$:Ce	700	98.79	−2.15	6.73	7.07	−72.28	99.04	3.32
	800	99.31	−1.27	3.13	3.38	−67.88	99.37	3.43
	850	99.15	−1.20	2.64	2.90	−65.56	99.19	3.39
	900	98.89	−1.34	3.84	4.07	−70.79	98.97	3.29

2.3. Sample characterization

The phase purity of the $MAlO_3$ (M = Y, La, Ce) and $YAlO_3$: Ce xerogels calcined at 700, 800, 850 and 900 °C were analyzed by means of X-ray diffractometer (DX-2700) with Cu Kα radiation at a wavelength of 1.5406 Å operated at 40 kV and 30 mA. The surface morphology of the $MAlO_3$ (M = Y, La, Ce) and $YAlO_3$: Ce xerogels calcined at 700 or 900 °C were characterized by field-emission scanning electron microscopy (FE-SEM) and transmission electron microscopy (TEM). UV–vis diffuse reflectance spectra of the samples were examined on a UV–visible spectrophotometer with an integrating sphere attachment using $BaSO_4$ as the reference. The photoluminescence properties were investigated at room temperature with a SHIMADZU RF-5301PC fluorescence spectrophotometer in the range of 200–800 nm by a 150 W xenon lamp as excitation source.

2.4. Photoelectrochemical measurement

The electrochemical properties of the $MAlO_3$ (M = Y, La, Ce) and $YAlO_3$: Ce xerogels calcined at 700 or 900 °C were investigated on a CST 350 electrochemical workstation using a three-electrode cell configuration as described in the literature [37]. In this experiments, the $MAlO_3$ (M = Y, La, Ce) and $YAlO_3$: Ce samples, a standard calomel electrode (SCE), and Pt were used as the working electrode, the
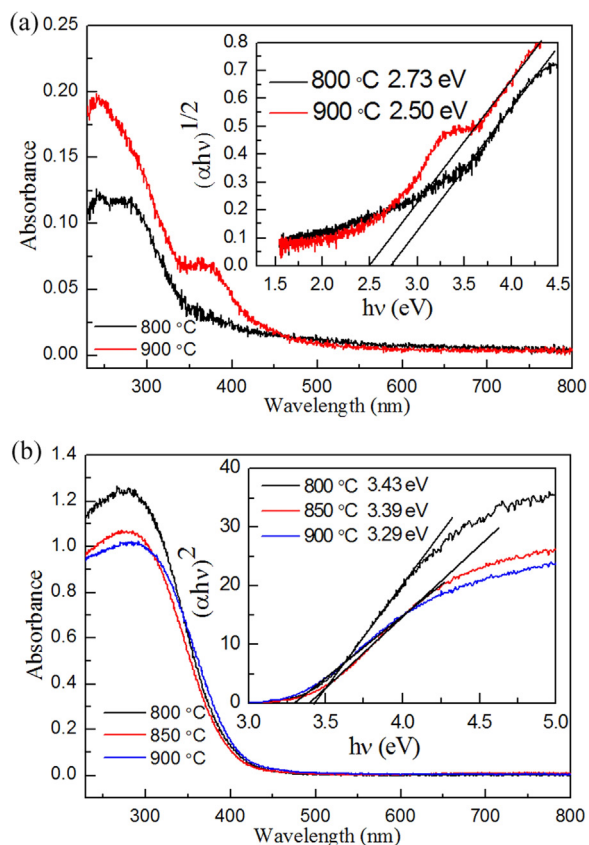
Fig. 5. UV–Vis absorption spectra of (a) $YAlO_3$ and (b) $YAlO_3$: Ce xerogels calcined at different temperatures. The inset shows the Eg values of the $YAlO_3$ and $YAlO_3$: Ce xerogels calcined at different temperatures, respectively.

reference electrode and the counter electrode, respectively. The working electrode included 15 mg of $MAlO_3$ (M = Y, La, Ce) or $YAlO_3$: Ce, 0.75 mg of polyvinylidene fluoride (PVDF), 0.75 mg of carbon black and 1-methyl-2-pyrrolidone (NMP) as solvent. The slurry evenly dispersed on the fluorine-doped tin oxide (FTO) glass substrate with area of 1 cm × 1 cm and transferred to the 60 °C thermostat drying oven for 5 h. 0.1 mol/L Na_2SO_4 aqueous solution (pH = 7) was applied as the electrolyte in all photoelectrochemical measurement. The electrochemical impedance spectroscopy (EIS) data were measured at different potentials in the frequency range from 10^{-2} to 10^5 Hz. The transient photocurrent response was measured at a bias potential of 0.2 V under light illumination using a 200 W xenon lamp.

3. Results and discussion

3.1. Structural analysis

Fig. 1 shows the XRD patterns of the $MAlO_3$ (M = Y, La, Ce) and $YAlO_3$: Ce xerogels calcined at 700 °C. For the $CeAlO_3$ and $LaAlO_3$ xerogels calcined at 700 °C, each sample shown only a single phase, and all of the diffraction peaks were ascribed to $CeAlO_3$ and $LaAlO_3$, as indexed in JCPDS Nos. 43-1002, and 31-0022, respectively. For the $YAlO_3$ and $YAlO_3$: Ce xerogels calcined at 700 °C, each powder exhibited a amorphous phase. The results indicate that a higher calcining temperature is needed for improving the phase purity of the $YAlO_3$ and $YAlO_3$: Ce samples.

$YAlO_3$ xerogel calcined at 800 and 900 °C were characterized by X-ray diffractometer in order to support the above conclusions obtained by Fig. 1. Fig. 2 shows the XRD patterns of the $YAlO_3$ xerogel calcined

at 800 and 900 °C. After being calcined at 800 °C, the powder is still noncrystalline with no obviously diffraction peaks except the large amorphous peak observed in Fig. 2. The $YAlO_3$ xerogel calcined at 900 °C contains a mixture of two phases, including hexagonal structure of $YAlO_3$ (JCPDF no. 16-0219) and orthorhombic structure of $Al_2Y_4O_9$ (JCPDF no. 14-0475).

Fig. 3 shows the XRD patterns of the $YAlO_3$: Ce sample prepared by adding a certain amount of Ce^{3+} ions into the precursor solution of $YAlO_3$ and then calcined at 800, 850, and 900 °C, respectively. It can be seen that a single phase $YAlO_3$ is formed at 800 °C. To further improve the crystallinity of the $YAlO_3$:Ce material, the calcining temperature is increased to 850 °C, thus leading to the formation of a mixed phases, including Ce_2O_3 (◆) and hexagonal structure of $YAlO_3$. When the calcining temperature further increases to 900 °C, $YAlO_3$:Ce material show similar crystalline characteristics with the sharp XRD diffraction peaks in Fig. 3. Accordingly, from the X-ray diffraction analysis results of Figs. 1, 2 and 3, one can draw a conclusion that the crystallization temperature of the $MAlO_3$ (M = Y, La, Ce) decreases with the increasing ion radius of trivalent metal ion M^{3+}. The results also indicate that the Ce^{3+} doping improved phase purity and dropped crystallization temperature of $YAlO_3$.

3.2. Optical properties

UV–vis diffuse reflectance spectra of the $MAlO_3$ (M = Y, La, Ce) and $YAlO_3$: Ce samples were measured on a UV–Visible spectrophotometer with an integrating sphere attachment. Fig. 4(a) shows the UV–vis diffuse reflectance spectra of the $MAlO_3$ (M = Y, La, Ce) and $YAlO_3$: Ce xerogels calcined at 700 °C. In the ultraviolet region, a continuous increase in reflectance for the $CeAlO_3$, $LaAlO_3$, $YAlO_3$ and $YAlO_3$: Ce samples are observed up to 510, 370, 380 and 480 nm, respectively. For the $LaAlO_3$ and $YAlO_3$ samples, a weak reflection peak at 259, and 264 nm was observed, respectively. The color parameters (L*, a*, b*), the hue angle, $H° = arctan$ (b^*/a^*), the total color difference, $\Delta E_{CIE}^* = \sqrt{(L^*)^2 + (a^*)^2 + (b^*)^2}$, and the chroma parameter (c*) of $MAlO_3$ (M = Y, La, Ce) and $YAlO_3$: Ce samples were calculated by literature [36] and were given in Table 1. Where, L*, a*, and b* are the lightness axis (black (0) to white (100)), the green (-) to red (+) axis, and the blue (-) to yellow (+) axis, respectively. As can be seen from Table 1, the L* and ΔE_{CIE}^* values of $MAlO_3$ samples increase with the decreasing the ion radius of trivalent metal ion M^{3+}. However, for the b* and c* values, the opposite. For the $LaAlO_3$ pigment, a similar color parameters are obtained by Pimentel et al. [9].

According to the UV–vis diffuse reflectance spectra, UV–Vis absorption spectra of $MAlO_3$ (M = Y, La, Ce) and $YAlO_3$: Ce samples were obtained by the Kubelka-Munk (K–M) formula,

$$F(R) = \frac{\alpha}{S} = \frac{(1 - R_\infty)^2}{2R} \tag{1}$$

where R, α, and S represents the reflectance, the absorption coefficient, and the scattering coefficient, respectively. Fig. 4(b) shows the UV–Vis absorption spectra of the $MAlO_3$ (M = Y, La, Ce) and $YAlO_3$: Ce xerogels calcined at 700 °C. For the $CeAlO_3$ sample, two obvious absorption peaks at 282 and 326 nm are ascribed to charge-transfer transition from oxygen to Ce^{3+} ions, and interband transitions in $CeAlO_3$, respectively [38–40]. For the $LaAlO_3$ and $YAlO_3$ samples, two obvious absorption peaks at 230 and 300/284 nm are observed. The former is assigned to charge transfer from the oxygen ligands to the central aluminum atom inside the AlO_3^{3-} [40,41] and the latter could be attributed to the charge-transfer transition from oxygen to La/Y ions [40,41]. For the $YAlO_3$: Ce sample, a strongly absorption peak at 282 nm can be also ascribed to charge-transfer transition from oxygen to Ce^{3+} ions.

In addition, the relationship between α and the band-gap energy (Eg) follows the equation:
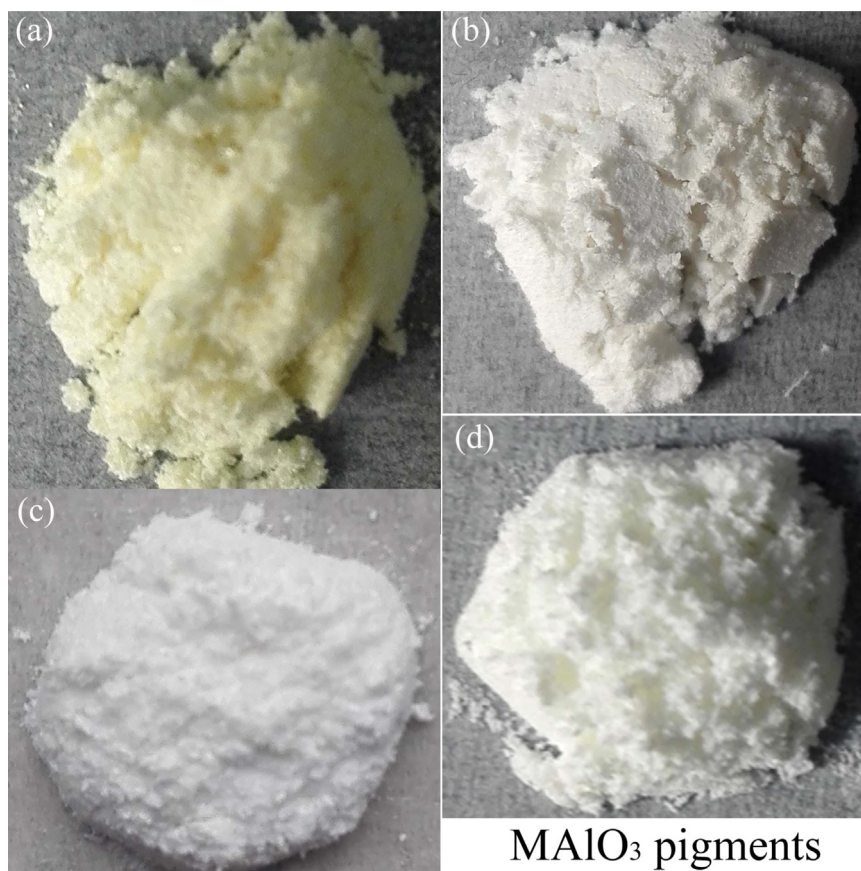
Fig. 6. The real photos of (a) CeAlO₃ and (b) LaAlO₃ xerogels calcined at 700 °C, and (c) YAlO₃ and (d) YAlO₃: Ce xerogels calcined at 900 °C.

$$(F(R)E)^n = A(E - E_g) \qquad (2)$$

where E, and A are photon energy and a proportionality constant, respectively. n is a value that highly depends on the nature of semiconductor (2 for a direct band gap semiconductor, and 1/2 for indirect band gap semiconductor). In this case, $CeAlO_3$ and Ce_2O_3 are direct band gap semiconductor [42,43], however, $YAlO_3$ and $LaAlO_3$ are indirect band gap semiconductor [44,45]. Fig. 4(c) and (d) shows the Eg values of the $MAlO_3$ (M=Y, La, Ce) and $YAlO_3$: Ce xerogels calcined at 700 °C and the Eg values are also given in Table 1. The Eg values of the $CeAlO_3$, $LaAlO_3$, $YAlO_3$ and $YAlO_3$: Ce samples are found to be 3.15, 1.64, 2.78, and 3.32 eV, respectively.

Fig. 5 shows the UV–Vis absorption spectra of the $YAlO_3$ and $YAlO_3$: Ce xerogels calcined at different temperatures. In Fig. 5(a), three obvious absorption peaks at 243, 284, and 359 nm for the $YAlO_3$ xerogel calcined at 800 °C are observed. The absorption peak at 284 nm can be assigned to the pure $YAlO_3$ i.e. the charge-transfer transition from oxygen to La/Y ions. Premkumar et al. [46] reported the peak at 280 nm arises due to a transition from valence band to conduction band. The absorption peaks at 243 and 358 nm may be ascribed to the $Al_2Y_4O_9$ in presence of the sample. When the $YAlO_3$ xerogel calcined at 900 °C, the intensity of two absorption peaks at 243 and 358 nm to become stronger due to the XRD diffraction peaks of the $Al_2Y_4O_9$ become very sharp (see Fig. 2). Fig. 5(a) inset shows the Eg values of the $YAlO_3$ xerogel calcined at different temperatures and the Eg values are also given in Table 1. As can be seen from the Table 1, the Eg values of the $YAlO_3$ decreases with the increasing the calcining temperature. The results are consistent with those obtained from literature [47,48]. In addition, L^*, a^*, b^*, c^*, H° and ΔE_{CIE}^* values vary randomly. When the

calcining temperature reach to 900 °C, the b^* and c^* values are biggest because of the enhancement in the crystallinity of the sample.

Fig. 5(b) presents the UV–Vis absorption spectra of the $YAlO_3$: Ce xerogels calcined at different temperatures. When the Ce^{3+} ions are introduced into the precursor solution, a red shift in the wavelength occurs in the absorption peak at about 280 nm. This is probably related to the Ce^{3+} ions improve surface morphology and reduce particle size of $YAlO_3$: Ce nanoparticles, and then leading to the quantum size effect, ultimately resulting in the absorption peak shifts to the longer wavelength. It can be also seen that the intensity of the absorption peak decreases with the increasing the calcining temperature due to the enhancement in the crystallinity of the sample. Fig. 5(b) inset shows the Eg values of the $YAlO_3$: Ce xerogel calcined at different temperatures and the Eg values are also given in Table 1. In addition, the L^*, a^*, b^*, c^*, H° and ΔE_{CIE}^* values are also calculated on the basis of the UV–vis diffuse reflectance spectra. When the calcining temperature increases from 800 to 900 °C, L^*, ΔE_{CIE}^* and Eg values decreases with the increasing the calcining temperature, however, a^*, b^*, c^* and H° values vary randomly. When the calcining temperature reach to 900 °C, the b^* and c^* values are also biggest due to the enhancement in the crystallinity of the sample.

Fig. 6 shows the real photos of (a) $CeAlO_3$ and (b) $LaAlO_3$ xerogels calcined at 700 °C, and (c) $YAlO_3$ and (d) $YAlO_3$: Ce xerogels calcined at 900 °C. For the $CeAlO_3$ xerogel calcined at 700 °C, presenting a bright yellow color, while $LaAlO_3$ crystallizes at same temperature, corresponding to the bright white color. For the $YAlO_3$ xerogel calcined at 900 °C, presenting a snowy white color, $YAlO_3$: Ce crystallizes at 900 °C, presenting an off-white color. The real photos of the $CeAlO_3$, $LaAlO_3$, $YAlO_3$ and $YAlO_3$: Ce samples are consistent with the color parameters
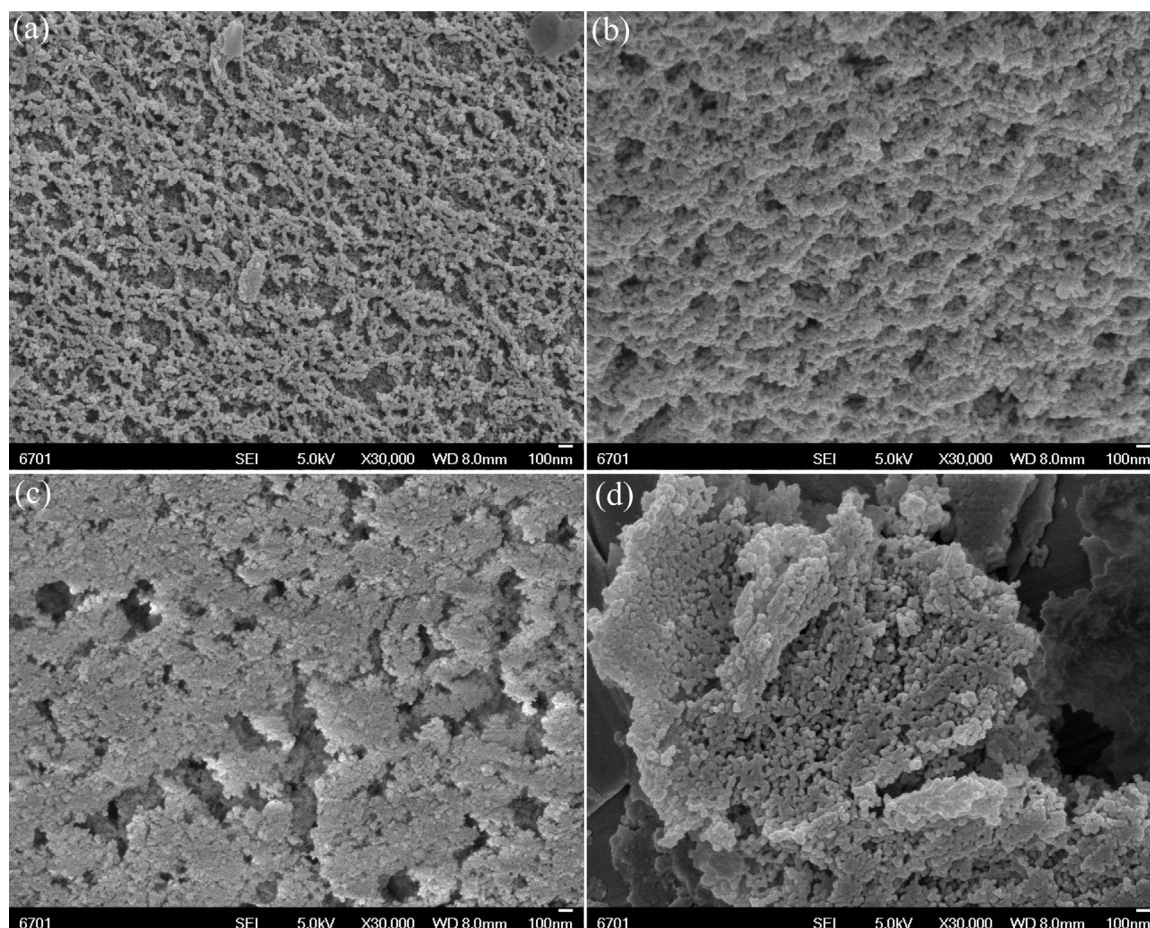
Fig. 7. SEM images of (a) CeAlO₃ and (b) LaAlO₃ xerogels calcined at 700 °C, and (c) YAlO₃ and (d) YAlO₃: Ce xerogels calcined at 900 °C.

as shown in Table 1. Pimentel and others sees lanthanide ions in the A site for MAlO₃ pigments have a small contribution on the color definition [9]. However, above results indicate that Ce³⁺ ion have a great contribution on the color definition. It can be explained that the deformation of unit cell of CeAlO₃ pigment increasing the electronic transitions 4f→5d in visible region because of the pseudo Jahn–Teller effect, and then more intense color is formed [49].

3.3. Surface morphology analysis

Fig. 7 shows the SEM images of the CeAlO₃ and LaAlO₃ xerogels calcined at 700 °C, and YAlO₃ and YAlO₃: Ce xerogels calcined at 900 °C. The SEM images show that the CeAlO₃ (see Fig. 7(a)) and LaAlO₃ (see Fig. 7(b)) particles are almost spherical in shape and have a narrow particle size distribution. However, more accurate information about the surface morphology of the CeAlO₃ and LaAlO₃ samples will be characterized by TEM. For the YAlO₃ sample, an obvious aggregation was observed in Fig. 7(c). When the Ce³⁺ ions are introduced into YAlO₃ precursor solution, the relatively minor agglomeration particles as shown in Fig. 7(d). The results indicate that the Ce³⁺ ions added into YAlO₃ precursor solution improves surface morphology of YAlO₃.

Fig. 8(a) shows a TEM image of the CeAlO₃ xerogel calcined at 700 °C. The TEM image confirmed that CeAlO₃ nano-crystals have a narrow particle size distribution and the average particle size is around 8 nm as shown in Fig. 8(b). Fig. 8(c) shows the selected area electron diffraction (SAED) pattern taken from a portion of the CeAlO₃ nano-crystals shown in Fig. 8(a). The SAED pattern indicated that the CeAlO₃

nanoparticles possess interplanar spacings of 3.1209, 2.7045, 1.9128, 1.6317, 1.5619, and 1.3526 Å corresponding to the (111), (200), (220), (311), (222), and (400) planes, respectively. A high resolution transmission electron microscopy (HRTEM) image of the CeAlO₃ xerogel calcined at 700 °C as show in Fig. 8(d). The HRTEM image indicated that the lattice spacing of 0.2710 nm between and among adjacent lattice planes corresponds to the *d*-spacing of (200) planes, 0.1938 nm corresponds to (220) planes, 0.1561 nm corresponds to (222) planes and 0.1241 nm corresponds to (331) planes. To further analysis the elemental composition of CeAlO₃ pigment, the energy dispersive spectrometer (EDS) of the CeAlO₃ xerogel calcined at 700 °C as shown in Fig. 8(e). As can be seen from Fig. 8(e), the major elemental composition of CeAlO₃ sample are Ce, Al, O, C, and Cu. The characteristic peaks of C, O, and Al elements appeared at 0.2455, 0.5267, and 1.4884 keV, respectively. The characteristic peaks of Ce element appeared at 0.6325, 0.7498, 1.1037, 4.2534, 4.9389, 5.4107, 5.6487, 6.1091, 6.5832, 34.3941, 34.7418 and 39.0734 keV. The characteristic peaks of Cu element appeared at 0.8695, 7.9688, and 8.7871 keV. The C and Cu elements are attributed to the TEM micromesh grid [50–52]. The results verified that a pure CeO₂ nanoparticle is completely formed after calcining at 700 °C.

Fig. 9(a) shows a TEM image of the LaAlO₃ xerogel calcined at 700 °C. The LaAlO₃ powders show continuously mesoporous and monolithic structures, further confirming that the polyacrylamide gel route can be employed to preparation the porous material [53,54]. The mean pore size of the LaAlO₃ porous material is about 20 nm. Fig. 9(b) shows the SAED pattern taken from a portion of the LaAlO₃ porous
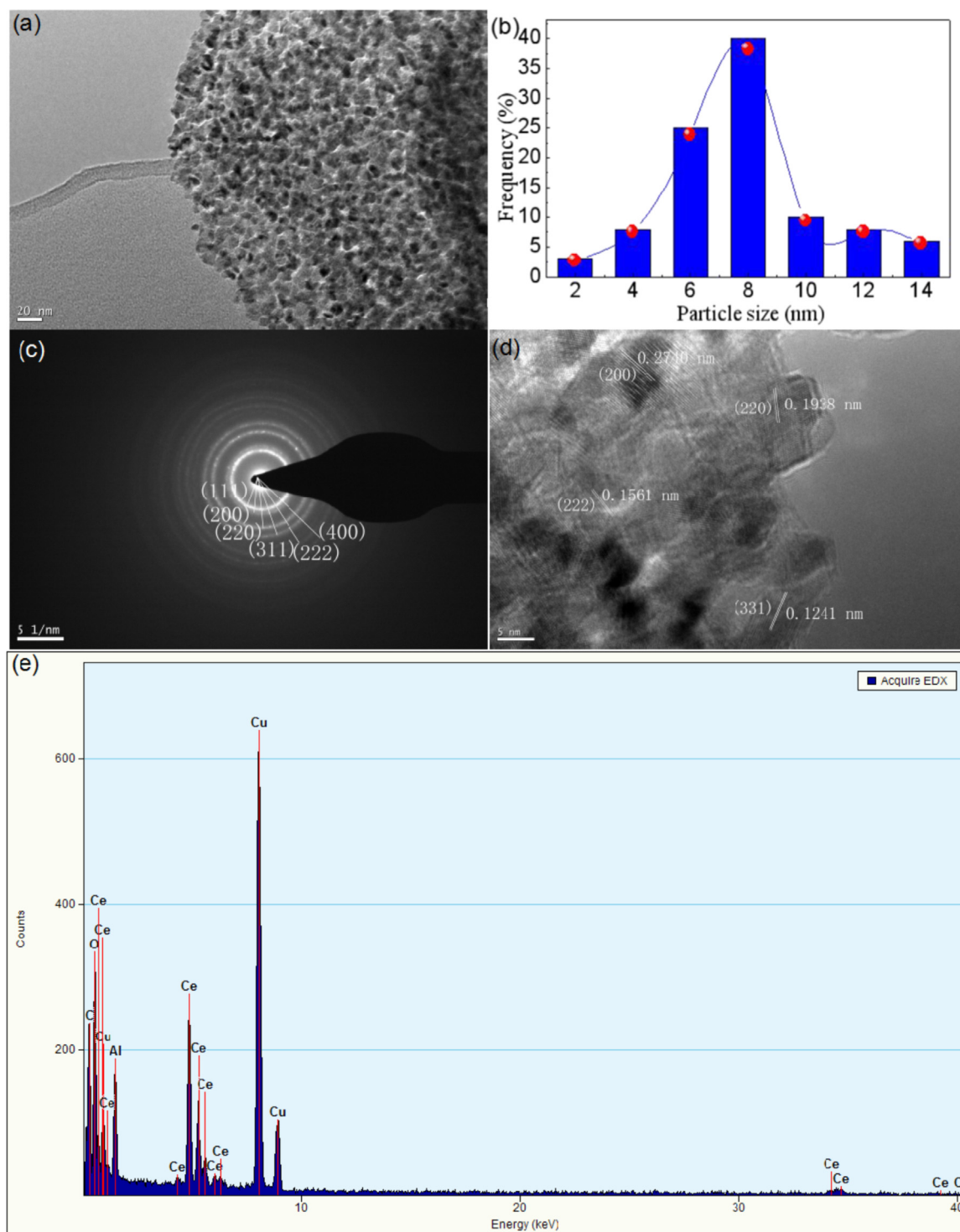
Fig. 8. (a) TEM image, (b) Particle size distribution, (c) SAED pattern, (d) HRTEM image and (e) energy dispersive spectrometer (EDS) of the CeAlO$_3$ xerogel calcined at 700 °C.

material shown in Fig. 9(a). The SAED pattern indicated that the perovskite type LaAlO$_3$ porous material possess interplanar spacings of 3.7915, 2.6871, and 1.5479 Å corresponding to the (012), (110), and (300) planes, respectively. In this case, no HRTEM image was observed. This results further indicate that the crystallization temperature of

MAlO$_3$ (M=Y, La, Ce) decreases with the increasing ion radius of trivalent metal ion M^{3+}. Further EDS analysis of the LaAlO$_3$ porous material as shown in Fig. 9(c), the results show that the major elemental composition of the LaAlO$_3$ porous material are La, C, Al, Cu and O. The characteristic peaks of C, O, Al and Cu elements are similar to the
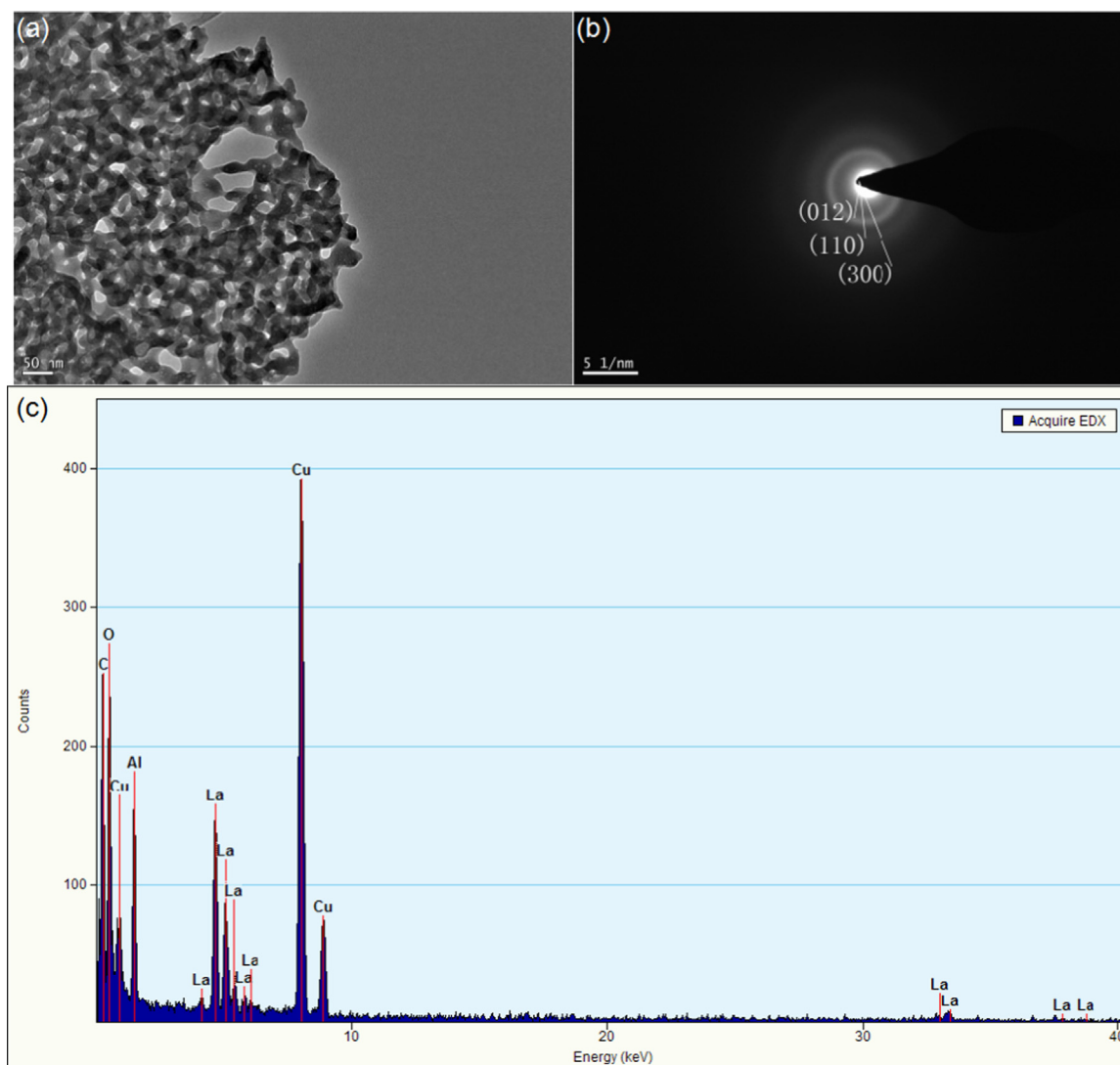
Fig. 9. (a) TEM image, (b) SAED pattern, and (c) energy dispersive spectrometer (EDS) of the LaAlO$_3$ xerogel calcined at 700 °C.

CeAlO$_3$ nanoparticles. The characteristic peaks of La element appeared at 4.1175, 4.6474, 5.0584, 5.3937, 5.8371, 6.0426, 33.0272, 33.5031, 37.8185 and 38.6621 keV. The results also indicated that the perovskite type LaAlO$_3$ porous material is completely formed after calcining at 700 °C.

3.4. Photoluminescence properties

Fig. 10(a) shows the emission spectra of CeAlO$_3$ xerogel calcined at 700 °C for three different excitation wavelengths, including 280, 290, and 300 nm. It can be seen that the intensity of emission peak decreases with the increasing of the excitation wavelength. For the YAlO$_3$: Ce sample, a similar variation tendencies are observed as shown in Fig. 10(b). The location of emission peaks remain unaltered under different excitation wavelength for the CeAlO$_3$ and YAlO$_3$: Ce samples. For the CeAlO$_3$ sample, the intensity of emission peak is maximum excited by the excitation wavelength about 290 nm. The emission spectrum of the CeAlO$_3$ sample are made up of four emission peaks in the wavelength range from 300 to 800 nm and can be resolved using

four Gaussian peaks at 378, 429, 468 and 480 nm as shown in Fig. 10(c). Arhipov et al. [55] reported that the large CeAlO$_3$ perovskite crystals prepared by czochralski and edge-defined film fed growth techniques exhibit two emission peaks at 378 and 429 nm, which can be assigned to the 5d^1–4f (^{2}F$_{5/2,7/2}$) radiative transitions of Ce^{3+} ions in CeAlO$_3$. Yin et al. [56] synthesized the CeAl$_{11}$O$_{18}$ by solid–state reaction method shows two emission peaks at 350 and 450 nm. The peaks at 350 and 450 nm are attributed to 4f-5d electron transitions of normal Ce^{3+} in CeAl$_{11}$O$_{18}$ crystal lattice and Ce-O$_{Me}$ associates, respectively [56]. In our experiments, two new emission peaks at 468 and 480 nm are observed. The peaks at 468 and 480 nm can be assigned to the hopping from different levels to the valence band and the transitions of oxygen vacancies to the corresponding ground states [57,58].

In Fig. 10(d), the emission spectra of the YAlO$_3$: Ce sample are resolved into three separate peaks at 369, 413 and 458 nm. The emission peak at 369 nm can be assigned to the 5d→4 f transition of Ce^{3+} ions [14,59,60]. The emission peaks at 413 and 458 nm can be ascribed to the luminescence band of *F* centers in YAlO$_3$ [12,13]. Alshourbagy et al. [14] synthesized the Ce^{3+} doped YAlO$_3$ crystal fibers by μ-pulling down
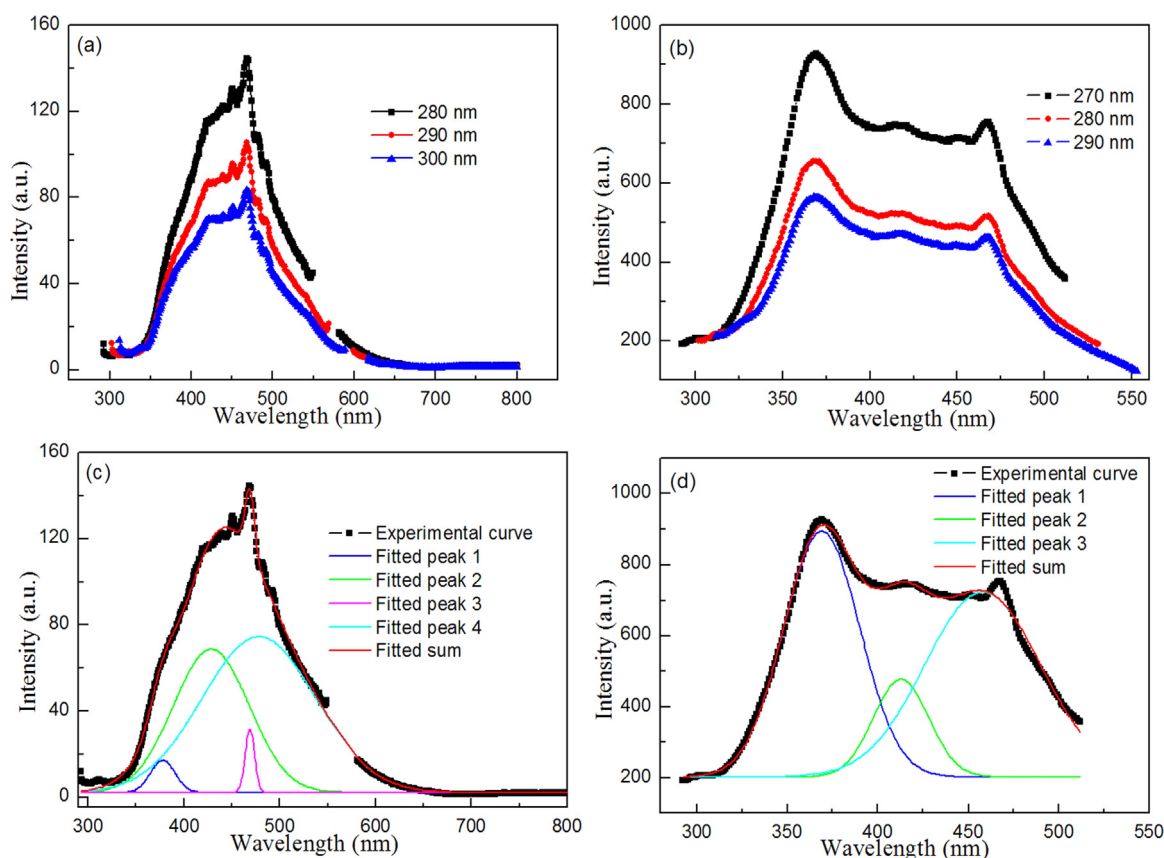
Fig. 10. Emission spectra of (a) $CeAlO_3$ and (b) $YAlO_3$: Ce xerogels calcined at 700 °C under different excitation wavelengths. (c) Emission spectrum of the $CeAlO_3$ xerogel calcined at 700 °C with the excitation wavelength at 280 nm could be resolved into four Gaussian peaks with the maxima at 378, 429, 468 and 480 nm, respectively. (d) Emission spectrum of the $YAlO_3$: Ce xerogel calcined at 700 °C with the excitation wavelength at 270 nm could be resolved into three Gaussian peaks with the maxima at 369, 413 and 458 nm, respectively.

technique shows a emission peak at 383 nm, which is ascribed to the transitions from the lowest crystal field components of $5d^1$ excited state to the $^2F_{5/2}$ and $^2F_{7/2}$ ground states. Parganiha et al. [15] reported that the $YAlO_3:Ce^{3+}$ powders prepared by solid state reaction method exhibits a broad emission band located from 419 to 495 nm. Xia et al. [16] prepared the $YAlO_3:Ce^{3+}$ powders by sol–gel combustion method shows a emission peak at 530 nm. Clearly, the emission spectra of the $YAlO_3$: Ce phosphors are strongly dependent on the synthetic route.

The emitting color was depicted by studying color coordinates of the $CeAlO_3$ and $YAlO_3$:Ce phosphors. The Commission International De I'Eclairage (CIE) diagram of the $CeAlO_3$ and $YAlO_3$:Ce phosphors under different excitation wavelengths are estimated from 1931 CIE system and are shown in Fig. 11. The CIE color coordinates (x, y) of the $CeAlO_3$ and $YAlO_3$:Ce phosphors under different excitation wavelengths were calculated using the corresponding emission spectra. The relative parameters of the $CeAlO_3$ and $YAlO_3$:Ce phosphors under different excitation wavelengths are shown in Table 2. It was observed that the CIE color coordinate (x, y) is found in blue region. For the $CeAlO_3$ phosphor, the CIE color coordinate (x, y) value increases with the increasing of the excitation wavelength as shown in Fig. 11(a) and Table 2. The y value of $YAlO_3$:Ce phosphor increases with the increasing of the excitation wavelength, however, the x value vary randomly (see Fig. 11(b) and Table 2). This results clearly indicate that the $CeAlO_3$ and $YAlO_3$:Ce phosphors can be employed for blue light emitting

applications.

3.5. Electrochemical measurement

To understand the effects of M^{3+} ion and Ce^{3+} doping on the photoelectric properties of the $MAlO_3$ (M=Y, La, Ce) and $YAlO_3$: Ce samples, electrochemical impedance spectroscopy (EIS) technology was applied to investigate the solid/electrolyte interfaces of the $MAlO_3$ (M=Y, La, Ce) and $YAlO_3$: Ce samples under UV light irradiation. EIS measurement of the $CeAlO_3$, $LaAlO_3$, $YAlO_3$ or $YAlO_3$: Ce electrode was conducted in a frequency range of 10^{-2} to 10^5 Hz. Fig. 12 is the EIS spectra of the (a) $CeAlO_3$, (b) $LaAlO_3$, (c) $YAlO_3$ and (d) $YAlO_3$: Ce samples. As can be seen from Fig. 12, a single semicircle is observed in the high frequency region for all samples. The semicircle can be ascribed to the charge-transfer resistance at the electrode/electrolyte interface [51,61,62]. The interfacial resistance is 3500 Ω for the $CeAlO_3$ sample, 30,000 Ω for the $LaAlO_3$ sample, 3000 Ω for the $YAlO_3$ sample, and 800 Ω for the $YAlO_3$: Ce sample. It is apparent that the $YAlO_3$: Ce sample have a lowest initial interfacial resistance than other perovskite aluminates. It is noted that the composite structure appears to decrease electrical resistivity and accelerate charge transfer rate [63].

To study the difference in the electronic properties of the $MAlO_3$ (M=Y, La, Ce) and $YAlO_3$: Ce electrodes, Mott- Schottky measurements were completed in the dark on the basis of the impedance technique
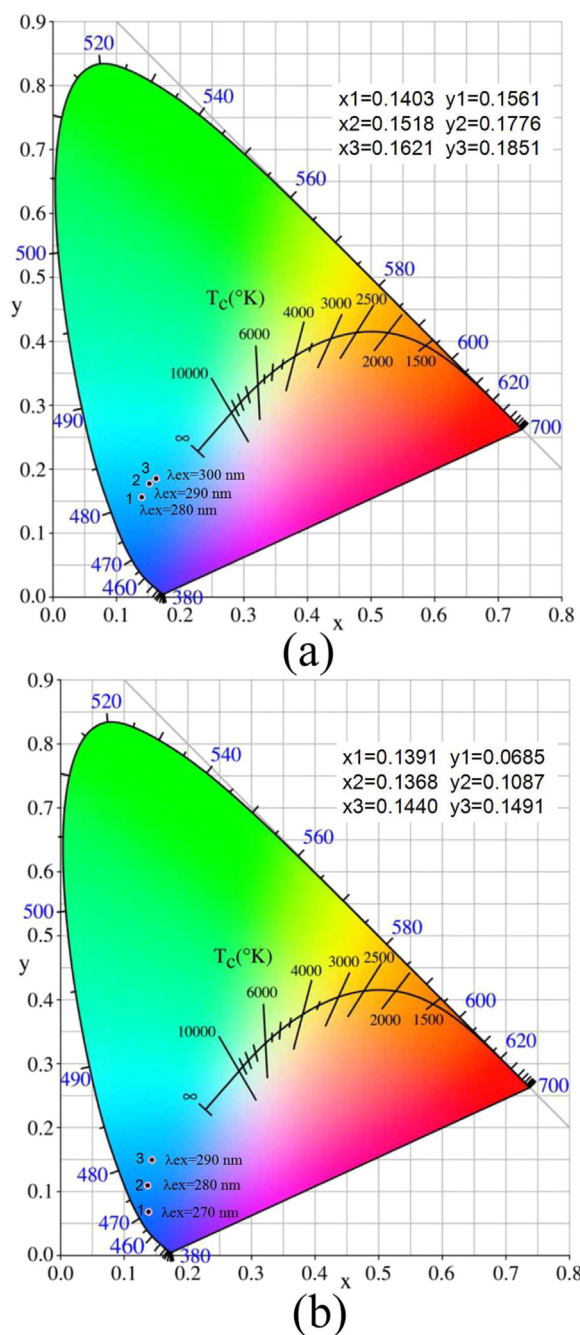
Fig. 11. CIE diagram of (a) CeAlO₃ and (b) YAlO₃: Ce xerogels calcined at 700 °C under different excitation wavelengths.

Table 2
CIE parameters of the CeAlO₃ and YAlO₃: Ce xerogels calcined at 700 °C for different excitation wavelengths.

Sample	Excitation Peak (nm)	CIE x	CIE y	Emission Peak (nm)	Peak Intensity
CeAlO₃	280	0.1403	0.1561	468	144.487
	290	0.1518	0.1776	468	105.456
	300	0.1621	0.1851	468	83.246
YAlO₃:Ce	270	0.1391	0.0685	369	927.002
	280	0.1368	0.1087	367	654.800
	290	0.1440	0.1491	368	564.512

[64]. Fig. 13 shows the flat-band potential (V_{fb}) for the (a) CeAlO₃, (b) LaAlO₃, (c) YAlO₃ and (d) YAlO₃: Ce samples as estimated from the Mott-Schottky plots deduced from the electrochemical measurements at 5000 Hz. For the CeAlO₃ and YAlO₃: Ce samples, a positive slope indicates that the CeAlO₃ and YAlO₃: Ce aluminates are n-type semiconducting materials, in agreement with the results of as reported [44]. For the LaAlO₃ and YAlO₃ samples, a negative slope suggests that the LaAlO₃ and YAlO₃ aluminates are p-type semiconducting materials, in agreement with the results of as reported [45,46]. According to the Fig. 13, the estimated V_{fb} values were -0.134, 1.845, 1.901, and 0.724 V vs. SCE for the CeAlO₃, LaAlO₃, YAlO₃ and YAlO₃: Ce samples, respectively. The potential at normal hydrogen electrode (NHE) can be described by Eq. (3) [65].

$$V(NHE) = V_{fb} + 0.059pH + 0.242 \qquad (3)$$

In this case, the pH = 8. The calculated V_{fb} values of the CeAlO₃, LaAlO₃, YAlO₃ and YAlO₃: Ce samples were found to be 0.580, 2.559, 2.615, and 1.438 V vs. NHE at pH = 0, respectively. For n or p type semiconducting materials, the difference between the conduction band (CB) edge potential or the valence band (VB) edge potential and the flat band potential can be ignored. The VB of the CeAlO₃ and YAlO₃: Ce samples are obtained as 3.730 and 4.728 V vs. NHE by considering its Eg values of 3.15 and 3.29 eV, respectively. The CB of the LaAlO₃ and YAlO₃ samples are calculated as 0.919 and 0.115 V vs. NHE by considering its Eg values of 1.64 and 2.50 eV, respectively.

Fig. 14 presents the photocurrent response of (a) CeAlO₃, (b) LaAlO₃, (c) YAlO₃ and (d) YAlO₃: Ce samples measured for various on-off cycles. For the n-type CeAlO₃ and YAlO₃: Ce samples, when xenon lamp was opened, rapidly increased of the photocurrent to a constant value. When xenon lamp was off, the photocurrent decreased to initial status sharply. After several on-off cycles, the photocurrent basically remained stable when the xenon lamp is on. For the p-type LaAlO₃ and YAlO₃ samples, an opposite phenomenon is observed. In general, the photocurrent density of the composite is bigger than the single phase. However, compared to YAlO₃:Ce sample (see Fig. 14(d)), YAlO₃ sample (see Fig. 14(c)) exhibits an enhanced photocurrent density, which is inconsistent with the previous reported. This phenomenon can be explained that the YAlO₃ sample is also mixed phases on the basis of XRD results.

4. Conclusions

Three different phases of M (M = Y, La, Ce) aluminates were successfully synthesized by a gamma-ray irradiation assisted polyacrylamide gel route. The result confirmed that the phase purity, surface morphology, and color, optical, photoluminescence and electrochemical properties of MAlO₃ pigments strongly dependent on the calcining temperature and trivalent metal ion M³⁺. XRD results indicate that the crystallization temperature of the MAlO₃ pigments decreases with the increasing ion radius of trivalent metal ion M³⁺. No direct relationship was concluded between particle size or Eg value of MAlO₃ pigments with trivalent metal ion M³⁺. Color parameters of the MAlO₃ pigments shows that the CeAlO₃ pigment have a strongest colors than other pigments may be due to the deformation of unit cell increasing the electronic transitions in visible region. The fluorescence spectra shows that four emission peaks at 378, 429, 468 and 480 nm are observed for the CeAlO₃ pigment when the excitation wavelength is 280 nm. The excellent photoluminescence properties of the CeAlO₃ pigment are attributed to the 5d¹–4 f ($^2F_{5/2,7/2}$) radiative transitions of Ce³⁺ ions and the transitions of oxygen vacancies to the corresponding ground states. Interesting, the Ce³⁺ doping improved phase purity, photoluminescence and electrochemical properties and dropped crystallization temperature of YAlO₃.
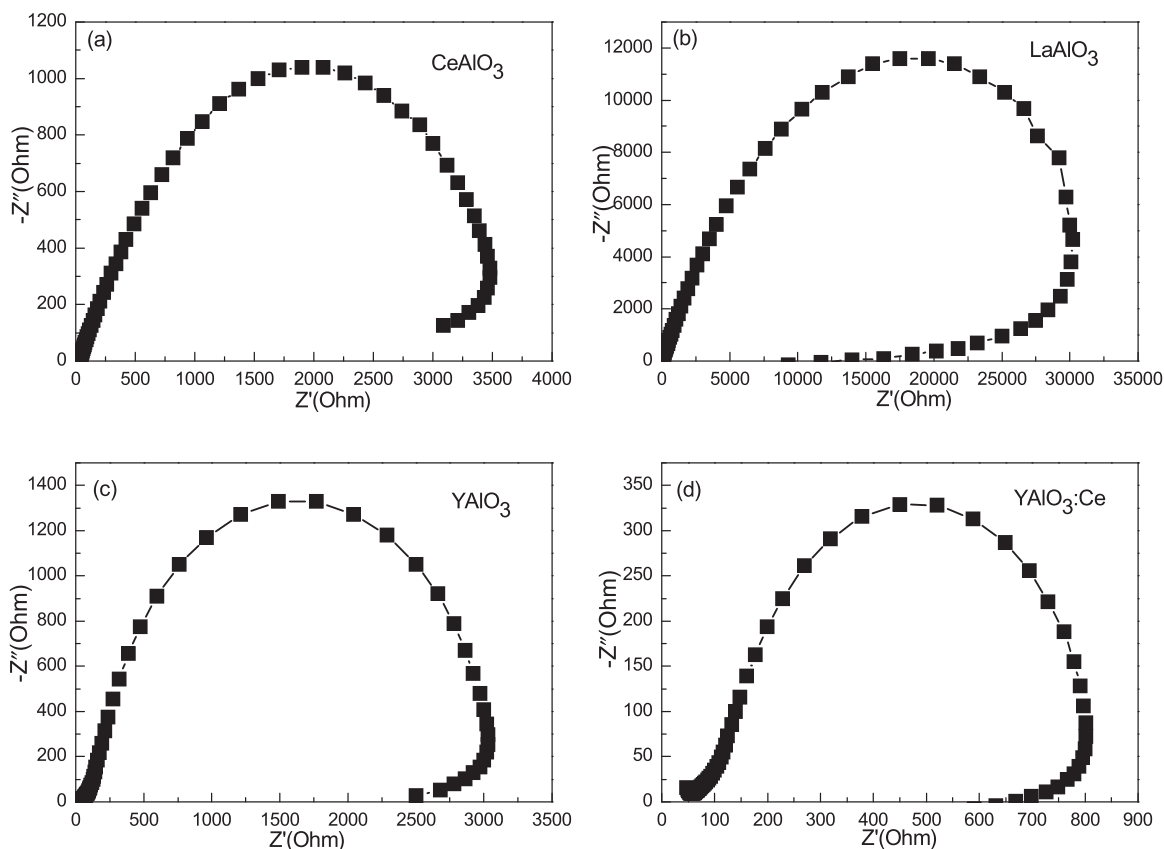
Fig. 12. EIS spectra of (a) CeAlO$_3$ and (b) LaAlO$_3$ xerogels calcined at 700 °C, and (c) YAlO$_3$ and (d) YAlO$_3$: Ce xerogels calcined at 900 °C.

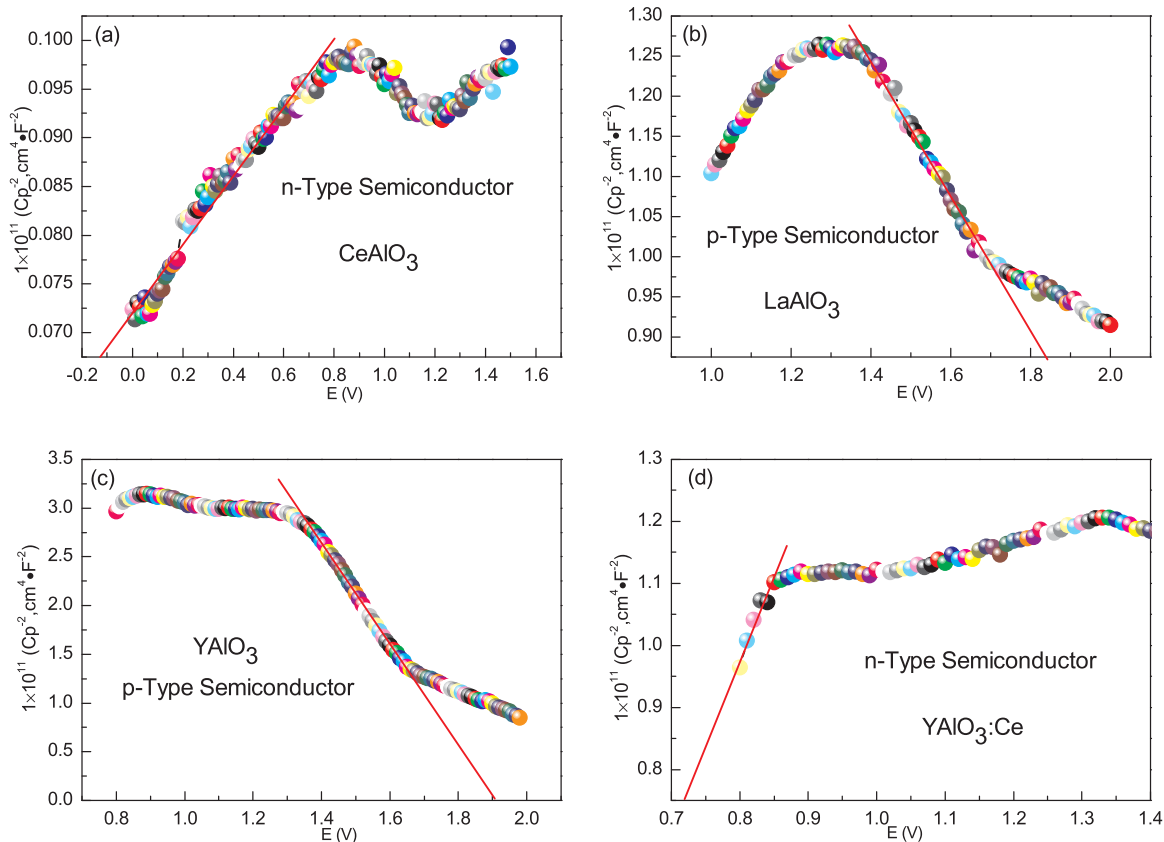**Fig. 13.** Mott–Schottky plots of (a) CeAlO$_3$ and (b) LaAlO$_3$ xerogels calcined at 700 °C, and (c) YAlO$_3$ and (d) YAlO$_3$: Ce xerogels calcined at 900 °C.
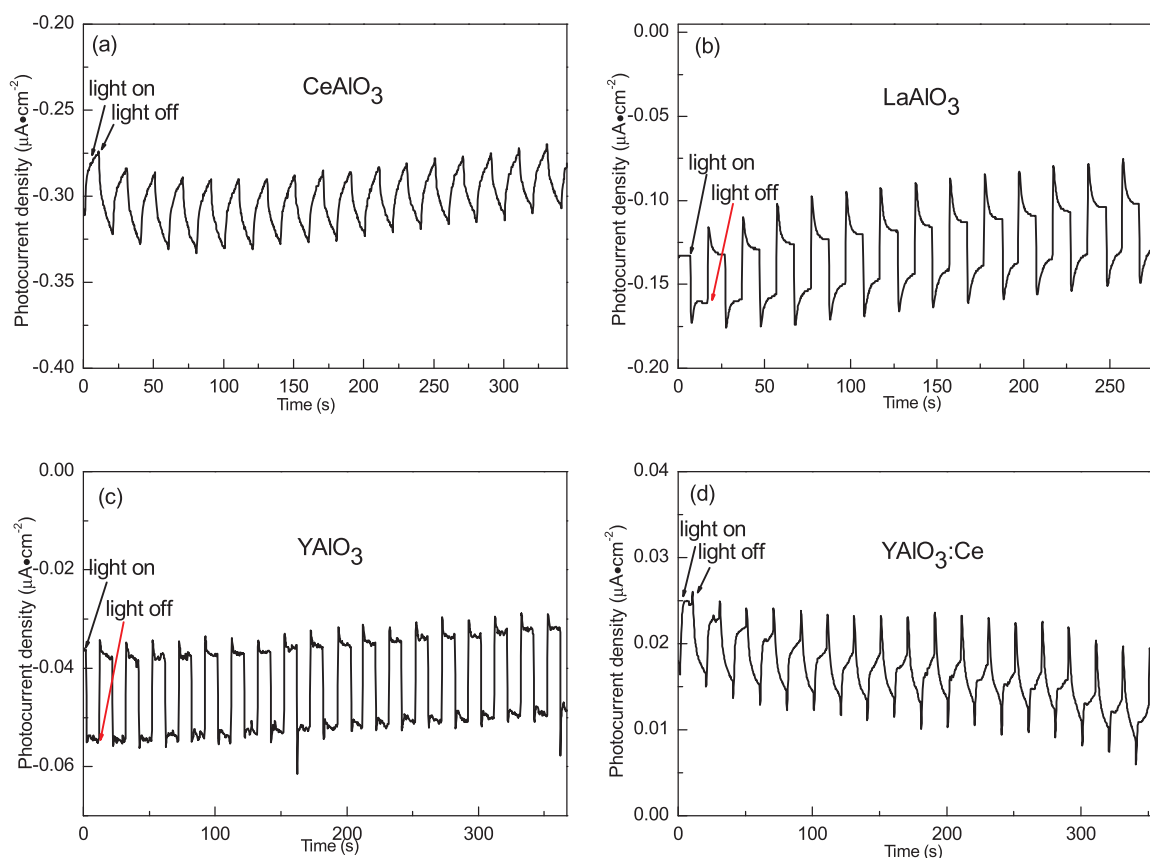
Fig. 14. Photocurrent response of (a) CeAlO₃ and (b) LaAlO₃ xerogels calcined at 700 °C, and (c) YAlO₃ and (d) YAlO₃: Ce xerogels calcined at 900 °C.

Acknowledgements

Conflict of interest

The authors declare that they have no competing interests.

References

[1] W.Y. Hernández, D. Lopez-Gonzalez, S. Ntais, C. Zhao, A. Boréave, P. Vernoux, Silver-modified manganite and ferrite perovskites for catalyzed gasoline particulate filters, Appl. Catal. B-Environ. 226 (2018) 202–212.

[2] N.O. Guldal, H.E. Figen, S.Z. Baykara, Perovskite catalysts for hydrogen production from hydrogen sulfide, Int. J. Hydrog. Energy 43 (2018) 1038–1046.

[3] S. Zeng, P. Kar, U.K. Thakur, K. Shankar, A review on photocatalytic CO₂ reduction using perovskite oxide nanomaterials, Nanotechnology 29 (2018) 052001.

[4] G.P. Mao, W. Wang, S. Shao, X.J. Sun, S.A. Chen, M.H. Li, H.M. Li, Research progress in electron transport layer in perovskite solar cells, Rare Met. 37 (2018) 95–106.

[5] Y. Sun, Q. Yang, H. Wang, X. Jiang, B. Li, Z. Shi, Luminescence properties of Pr³⁺ doped (Y₀.₉La₀.₁)₂O₃ transparent ceramics for potential applications in white LEDs and scintillators, J. Lumin. 194 (2018) 452–455.

[6] R. Diehl, G. Brandt, Crystal structure refinement of YAlO₃, a promising laser material, Mater. Res. Bull. 10 (1975) 85–90.

[7] G. Cheng, A. Annadi, S. Lu, H. Lee, J.W. Lee, M. Huang, J. Levy, Shubnikov-de haas-like quantum oscillations in artificial one-dimensional LaAlO₃/SrTiO₃ electron channels, Phys. Rev. Lett. 120 (2018) 076801.

[8] G. Lee, I. Kim, I. Yang, J.M. Ha, H.B. Na, J.C. Jung, Effects of the preparation method on the crystallinity and catalytic activity of LaAlO₃ perovskites for oxidative coupling of methane, Appl. Surf. Sci. 429 (2018) 55–61.

[9] P.M. Pimentel, S.V.M. Lima, A.F. Costa, M.S.C. Câmara, J.D.C. Carregosa, R.M.P.B. Oliveira, Gelatin synthesis and color properties of (La, Pr, Nd) lanthanide aluminates, Ceram. Int. 43 (2017) 6592–6596.

[10] S.S. Sreejith, N. Mohan, M.P. Kurup, Experimental and theoretical analysis of a rare nitrato bridged 3d-4f complex containing LaZn₂ core synthesized from a Zn (II) metalloligand, J. Mol. Struct. 1153 (2018) 85–95.

[11] C. Xu, H. Guan, Y. Song, Z. An, X. Zhang, X. Zhou, H. Zou, Novel highly efficient single-component multi-peak emitting aluminosilicate phosphors co-activated with Ce³⁺, Tb³⁺ and Eu²⁺: luminescence properties, tunable color, and thermal properties, Phys. Chem. Chem. Phys. 20 (2018) 1591–1607.

[12] Y.V. Zorenko, A.S. Voloshinovskii, G.B. Striganyuk, V.I. Gorbenko, Exciton luminescence of YAlO₃ single crystals and single-crystal films, Opt. Spectrosc. 98 (2005) 555–558.

[13] V. Babin, P. Fabeni, A. Krasnikov, K. Nejezchleb, M. Nikl, G.P. Pazzi, T. Savikhina, S. Zazubovich, Irregular Ce³⁺ and defect-related luminescence in YAlO₃ single crystal, J. Lumin. 124 (2007) 273–278.

[14] M. Alshourbagy, S. Bigotta, D. Herbert, A. Del Guerra, A. Toncelli, M. Tonelli, Optical and scintillation properties of Ce³⁺ doped YAlO₃ crystal fibers grown by μ-pulling down technique, J. Cryst. Growth 303 (2007) 500–505.

[15] Y. Parganiha, J. Kaur, V. Dubey, R. Shrivastava, YAlO₃: Ce³⁺ powders: synthesis, characterization, thermoluminescence and optical studies, Superlattices Microstruct. 85 (2015) 410–417.

[16] G. Xia, S. Zhou, J. Zhang, J. Xu, Structural and optical properties of YAG: Ce³⁺ phosphors by sol–gel combustion method, J. Cryst. Growth 279 (2005) 357–362.

[17] H. Wang, L. Zhang, C. Hu, X. Wang, L. Lyu, G. Sheng, Enhanced degradation of organic pollutants over Cu-doped LaAlO₃ perovskite through heterogeneous Fenton-like reactions, Chem. Eng. J. 33 (2018) 572–581.

[18] N. Alves, A. Kadari, W.B. Ferraz, L.O. de Faria, Thermoluminescence of LaAlO₃: C crystals grown by different mixing methodologies applied to UV dosimetry, Optik 153 (2018) 109–116.

[19] B. Basavalingu, H.N. Girish, K. Byrappa, K. Soga, Hydrothermal synthesis and characterization of orthorhombic yttrium aluminum perovskites (YAP), Mater. Chem. Phys. 112 (2008) 723–725.

[20] P.J. Dereń, B. Bondzior, G. Banach, B. Brzostowski, How the size of LaAlO₃ nanocrystals changes its spectroscopic properties, J. Lumin. 193 (2018) 73–78.

[21] R. Ianos, R. Lazǎ̆u, R. Borcǎ̆nescu, R. Ba̅but, Single-step combustion synthesis of YAlO₃ powders, J. Mater. Sci. 50 (2015) 6382–6638.

[22] F. Liu, J. Huang, J. Jiang, Synthesis and characterization of red pigment YAl₁₋ᵧCrᵧO₃ prepared by the low temperature combustion method, J. Eur. Ceram. Soc. 33 (2013) 2723–2729.

[23] P. Yadav, A.A. Muley, C.P. Yoshy, S.V. Moharil, P.L. Muthal, S.M. Dhopte, Combustion synthesis of compounds in the Y₂O₃-Al₂O₃ system, Int. J. Self-Propag. High-Temp. Synth. 21 (2012) 124–133.

[24] S.T. Aruna, N.S. Kini, S. Shetty, K.S. Rajam, Synthesis of nanocrystalline CeAlO₃ by solution-combustion route, Mater. Chem. Phys. 119 (2010) 485–489.

[25] M. Medraj, R. Hammond, M.A. Parvez, R.A.L. Drew, W.T. Thompson, High temperature neutron diffraction study of the Al₂O₃–Y₂O₃ system, J. Eur. Ceram. Soc. 26 (2006) 3515–3524.

[26] E. Caponetti, S. Enzo, B. Lasio, M.L. Saladino, Co-precipitation synthesis of

neodymium-doped yttrium aluminium oxides nanopowders: quantitative phase investigation as a function of joint isothermal treatment conditions and neodymium content, Opt. Mater. 29 (2007) 1240–1243.

[27] W. Li, M.W. Zhuo, J.L. Shi, Synthesizing nano $LaAlO_3$ powders via co-precipitation method, Mater. Lett. 58 (2004) 365–368.

[28] T.B. de Queiroz, C.R. Ferrari, D. Ulbrich, R. Doyle, A.S.S. de Camargo, Luminescence characteristics of YAP: Ce scintillator powders and composites, Opt. Mater. 32 (2010) 1480–1484.

[29] M.A. Małecka, L. Kępiński, New, intermediate polymorph of $CeAlO_3$ with hexagonal structure–formation and thermal stability, CrystEngComm 17 (2015) 2273–2278.

[30] A. Douy, P. Odier, The polyacrylamide gel: a novel route to ceramic and glassy oxide powders, Mater. Res. Bull. 24 (1989) 1119–1126.

[31] M. Kakihana, T. Okubo, Low temperature powder synthesis of $LaAlO_3$ through in situ polymerization route utilizing citric acid and ethylene glycol, J. Alloy. Compd. 266 (1998) 129–133.

[32] S.F. Wang, X.T. Zu, G.Z. Sun, D.M. Li, C.D. He, X. Xiang, W. Liu, S.B. Han, S. Li, Highly dispersed spinel (Mg, Ca, Ba)-ferrite nanoparticles: tuning the particle size and magnetic properties through a modified polyacrylamide gel route, Ceram. Int. 42 (2016) 19133–19140.

[33] Y.C. Ye, H. Yang, R.S. Li, X.X. Wang, Enhanced photocatalytic performance and mechanism of Ag-decorated $LaFeO_3$ nanoparticles, J. Sol-Gel Sci. Technol. 82 (2017) 509–518.

[34] L.J. Di, H. Yang, T. Xian, X.J. Chen, Enhanced photocatalytic activity of $NaBH_4$ reduced $BiFeO_3$ nanoparticles for rhodamine B decolorization, Materials 10 (2017) 1118.

[35] S.F. Wang, D.M. Li, C.Q. Yang, G.G. Sun, J. Zhang, Y.H. Xia, C.M. Xie, G.X. Yang, M. Zhou, W. Liu, A novel method for the synthesize of nanostructured $MgFe_2O_4$ photocatalysts, J. Sol-Gel Sci. Technol. 84 (2017) 169–179.

[36] H.J. Gao, H. Yang, S.F. Wang, D.M. Li, F. Wang, L.M. Fang, L. Lei, Y.H. Xiao, G.X. Yang, A new route for the preparation of $CoAl_2O_4$ nanoblue pigments with high uniformity and its optical properties, J. Sol-Gel Sci. Technol. 86 (2018) 206–216.

[37] C.X. Zheng, H. Yang, Z.M. Cui, H.M. Zhang, X.X. Wang, A novel $Bi_4Ti_3O_{12}/Ag_3PO_4$ heterojunction photocatalyst with enhanced photocatalytic performance, Nanoscale Res. Lett. 12 (2017) 608.

[38] D. Matei, D.S. Ezeanu, D. Cursaru, The efficiency of Co/CeO_2 catalyst in ethanol steam reforming process, Rev. Chim.-Buchar. 68 (2017) 2601–2604.

[39] S.F. Wang, C. Zhang, G. Sun, B. Chen, X. Xiang, H. Wang, L.M. Fang, Q. Tian, Q.P. Ding, X.T. Zu, Fabrication of a novel light emission material $AlFeO_3$ by a modified polyacrylamide gel route and characterization of the material, Opt. Mater. 36 (2013) 482–488.

[40] B. Chen, J. Yu, X. Liang, $LaAlO_3$ hollow spheres: synthesis and luminescence properties, Langmuir 27 (2011) 11654–11659.

[41] V. Singha, R.P.S. Chakradharb, J.L. Raoc, J.J. Zhua, Studies on red-emitting Cr^{3+} doped barium aluminate phosphor obtained by combustion process research, Mater. Chem. Phys. 111 (2008) 143–148.

[42] N. Shehata, K. Meehan, M. Hudait, N. Jain, S. Gaballah, Study of optical and structural characteristics of ceria nanoparticles doped with negative and positive association lanthanide elements, J. Nanomater. 2014 (2014) 156.

[43] X. Wang, H. Yamada, K. Nishikubo, C.N. Xu, Synthesis and electric property of $CeAlO_3$ ceramics, Jpn. J. Appl. Phys. 44 (2005) 961.

[44] G. Pari, A. Mookerjeee, A.K. Bhattacharya, Study of α-Al_2O_3 and the role of Y in $YAlO_3$ and $Y_3Al_5O_{12}$ by first principles electronic structure calculations, Physica B 353 (2004) 192–200.

[45] G. Murtaza, I. Ahmad, Shift of indirect to direct bandgap and optical response of $LaAlO_3$ under pressure, J. Appl. Phys. 111 (2012) 123116.

[46] H.B. Premkumar, D.V. Sunitha, H. Nagabhushana, S.C. Sharma, B.M. Nagabhushana, J.L. Rao, K. Guptad, R.P.S. Chakradhar, $YAlO_3$: Cr^{3+} nanophosphor: synthesis, photoluminescence, EPR, dosimetric studies, Spectrochim.

Acta A 96 (2012) 154–162.

[47] P.P. Shang, B.P. Zhang, J.F. Li, N. Ma, Effect of sintering temperature on thermoelectric properties of La-doped $SrTiO_3$ ceramics prepared by sol–gel process and spark plasma sintering, Solid State Sci. 12 (2010) 1341–1346.

[48] T. Vossmeyer, L. Katsikas, M. Giersig, I.G. Popovic, K. Diesner, A. Chemseddine, A. Eychmueller, H. Weller, CdS nanoclusters: synthesis, characterization, size dependent oscillator strength, temperature shift of the excitonic transition energy, and reversible absorbance shift, J. Phys. Chem. 98 (1994) 7665–7673.

[49] W.J.A. Maaskant, A cooperative pseudo Jahn-Teller effect in three phases of $CeAlO_3$, J. Mol. Struct. 838 (2007) 232–237.

[50] H.J. Gao, H. Yang, G.X. Yang, S.F. Wang, Effects of oxygen vacancy and sintering temperature on the photoluminescence properties and photocatalytic activity of CeO_2 nanoparticles with high uniformity, Mater. Technol. 33 (2018) 321–332.

[51] Z.M. Cui, H. Yang, X.X. Zhao, Enhanced photocatalytic performance of g-C_3N_4/$Bi_4Ti_3O_{12}$ heterojunction, Mater. Sci. Eng. B-Adv. 229 (2018) 160–172.

[52] F. Wang, H. Yang, Y.C. Zhang, Enhanced photocatalytic performance of $CuBi_2O_4$ particles decorated with Ag nanowires, Mater. Sci. Semicond. Proc. 73 (2018) 58–66.

[53] C. Lalanne, G. Prosperi, J.M. Bassat, F. Mauvy, S. Fourcade, P. Stevens, M. Zahid, S. Diethelm, J. Van herle, J.C. Grenier, Neodymium-deficient nickelate oxide $Nd_{1.95}NiO_{4+\sigma}$ as cathode material for anode-supported intermediate temperature solid oxide fuel cells, J. Power Sources 185 (2008) 1218–1224.

[54] M. Zhou, X.T. Zu, K. Sun, W. Liu, X. Xiang, Enhanced photocatalytic hydrogen generation of nano-sized mesoporous $InNbO_4$ crystals synthesized via a poly-acrylamide gel route, Chem. Eng. J. 313 (2017) 99–108.

[55] P. Arhipov, S. Tkachenko, I. Gerasymov, O. Sidletskiy, K. Hubenko, S. Vasyukov, N. Shiran, V. Baumer, P. Mateychenko, A. Fedorchenko, Y. Zorenko, Y. Zhydachevskii, K. Lebbou, M. Korjik, Growth and characterization of large $CeAlO_3$ perovskite crystals, J. Cryst. Growth 430 (2015) 116–121.

[56] L.J. Yin, G.Z. Chen, C. Wang, X. Xu, L.Y. Hao, H.T.B. Hintzen, Tunable luminescence of $CeAl_{11}O_{18}$ based phosphors by replacement of $(AlO)^+$ by $(SiN)^+$ and co-doping with Eu, ECS J. Solid State Sci. 3 (2014) R131–R138.

[57] P.J. Hay, R.L. Martin, J. Uddin, G.E. Scuseria, Theoretical study of CeO_2 and Ce_2O_3 using a screened hybrid density functional, J. Chem. Phys. 125 (2006) 34712.

[58] S. Aškrabić, Z.D. Dohčević-Mitrović, V.D. Araújo, G. Ionita, M.M. de Lima, A. Cantarero, F-centre luminescence in nanocrystalline CeO_2, J. Phys. Appl. Phys. 46 (2013) 495306.

[59] Y. Zorenkoa, V. Gorbenko, I. Konstankevych, T. Voznjak, V. Savchyn, M. Nikl, J.A. Mares, K. Nejezchle, V. Mikhailin, V. Kolobanov, D. Spassky, Peculiarities of luminescence and scintillation properties of YAP:Ce and LuAP:Ce single crystals and single crystalline films, Radiat. Meas. 42 (2007) 528–532.

[60] X.D. Wang, H.M. Mao, C.L. Ma, J. Xu, X.H. Zeng, Effects of Ce^{3+} energy level structure on absorption and luminescence properties of Ce-doped $YAlO_3$, $Y_3Al_5O_{12}$, and $LaAlO_3$ single crystals, Chin. Opt. Lett. 10 (2012) 071601.

[61] X.X. Wang, Y. Li, M.C. Liu, L.B. Kong, Fabrication and electrochemical investigation of MWO_4 (M = Co, Ni) nanoparticles as high-performance anode materials for lithium-ion batteries, Ionics 24 (2018) 363–372.

[62] X. Zhao, H. Yang, Z. Cui, R. Li, W. Feng, Enhanced photocatalytic performance of Ag–$Bi_4Ti_3O_{12}$ nanocomposites prepared by a photocatalytic reduction method, Mater. Technol. 32 (2017) 870–880.

[63] S. Kang, Y. Li, M. Wu, M. Cai, P.K. Shen, Synthesis of hierarchically flower-like $FeWO_4$ as high performance anode materials for Li-ion batteries by a simple hydrothermal process, Int. J. Hydrog. Energy 39 (2014) 16081–16087.

[64] G. Huang, Y. Zhu, Synthesis and photoactivity enhancement of $ZnWO_4$ photocatalysts doped with chlorine, CrystEngComm 14 (2012) 8076–8082.

[65] F. Wang, H. Yang, H.M. Zhang, J.L. Jiang, Growth process and enhanced photocatalytic performance of $CuBi_2O_4$ hierarchical microcuboids decorated with AuAg alloy nanoparticles, J. Mater. Sci. -Mater. Electron 29 (2018) 1304–1316.